Chinese Chemical Letters 35 (2024) 108482

Contents lists available at ScienceDirect

Chinese Chemical Letters

journal homepage: www.elsevier.com/locate/cclet

A scalable one-pot strategy for the development of polymer electrolytes adaptable to room-temperature high-voltage lithium batteries

Yue Guo[a], Xinxin Qu[a], Zhen Li[a], Ruiyuan Tian[b], Xiaokong Liu[a,*]

[a] *State Key Laboratory of Supramolecular Structure and Materials, College of Chemistry, Jilin University, Changchun 130012, China*
[b] *Key Laboratory of Physics and Technology for Advanced Batteries (Ministry of Education), College of Physics, Jilin University, Changchun 130012, China*

ARTICLE INFO

Article history:
Received 17 January 2023
Revised 16 March 2023
Accepted 19 April 2023
Available online 23 April 2023

Keywords:
Lithium batteries
Polymer electrolytes
Poly(ethylene oxide)
Energy density
High-voltage cathodes

ABSTRACT

Poly(ethylene oxide) (PEO) polymer electrolytes (PEs) have been commercially applied in $LiFePO_4||Li$ solid-state lithium batteries (SSLBs). However, it remains challenging to develop PEO-based PEs applicable to the high-voltage SSLBs with higher energy density, owing to the poor electrochemical stability of PEO. Herein, we report a scalable strategy for fabricating PEO-based PEs with high-voltage compatibility, by exploiting a new mechanism to stabilize the cathode-electrolyte interface in the high-voltage SSLBs. The protocol only involves a one-pot synthesis procedure to covalently crosslink the PEO chains, in the presence of high-content lithium bis(trifluoromethylsulphonyl)imide (LiTFSI) salts and *N*,*N*-dimethylformamide (DMF). LiTFSI-DMF supramolecular aggregates are formed and firmly embedded in the polymer network, endowing the PE with high room-temperature ionic conductivity. The dissociated and highly concentrated $TFSI^-$ anions can enter the Helmholtz layer close to the high-voltage cathode, leading to the formation of a thin and homogeneous cathode electrolyte interface (CEI), mainly composed of LiF, on the cathode. The CEI with high electrochemical stability can effectively stabilize the cathode-electrolyte interface, enabling long-term stable cycling of the high-voltage $LiCoO_2||Li$ and nickel-rich $NCM_{622}||Li$ batteries at room temperature. The simplicity and scalability of the strategy makes the reported PEO-based PE potentially applicable in high-voltage SSLBs in practice.

Solid-state lithium batteries (SSLBs), possessing advantages in terms of enhanced safety and energy density, have been regarded as one of the most promising alternatives to state-of-the-art lithium-ion batteries [1–7]. The solid-state electrolyte is one of the key components of SSLBs, playing dual roles to transfer Li^+ as well as separate the anodes and cathodes [8]. However, it is highly challenging and of high cost to process the inorganic solid-state electrolytes (*e.g.*, oxide/sulfide-based ones) into films/pallets for the scalable production of SSLBs [5,9–11]. Compared to the inorganic solid-state electrolytes, polymer electrolytes (PEs) are easy to be processed in large scales because of their intrinsic processability and good film forming features [6,9,11–16]. Among different types of PEs, poly(ethylene oxide) (PEO) electrolytes have gained widespread interests because of their low cost, easiness to process, in combination with their acceptable anodic stability and outstanding performance for solvating alkaline salt [15,17–21]. Due to these merits, PEO-based $LiFePO_4||Li$ SSLBs have been exploited in pure electric vehicles and commercialized by the Bolloré Group since 2011 [22,23]. However, these batteries have to be operated at 70–80 °C, because of the low room-temperature ionic conductivity of the PEO electrolytes [17,24–26]. Moreover, the energy density (*i.e.*, specific energy) of a battery is collectively determined by its specific capacity and operation voltage [27–30]. According to the formula of the specific energy $E = CV$, where C is the specific capacity and V is the operation voltage of a battery, replacing $LiFePO_4$ by the high-voltage cathodes (>4 V *vs.* Li/Li^+), such as $LiCoO_2$ and nickel-rich $Li(Ni_xCo_yMn_{1-x-y})O_2$ (NCM, $x \geq 0.6$), can remarkably enhance the energy density of the battery [27,31–34]. Unfortunately, the narrow electrochemical stability window (ESW) of PEO electrolytes (<4 V) restricts their combination with the high-voltage cathodes, which significantly limits their application in the high-voltage SSLBs with higher energy density [26,35,36]. Therefore, it is essential to make significant research efforts to develop PEO-based PEs that are applicable to the high-voltage cathodes for 4 V-class SSLBs.

Strategies, including cathode surface modification and construction of double/multi-layered structures, have been developed

---

[*] Corresponding author.
E-mail address: xiaokongliu@jlu.edu.cn (X. Liu).

https://doi.org/10.1016/j.cclet.2023.108482

to make the PEO-based PEs adaptable to the high-voltage cathodes [23,37–52]. The former approach is to coat the cathode particles (*e.g.*, $LiCoO_2$) with inert inorganic Li^+ conductors (*e.g.*, $Li_{1+x}Al_xTi_{2-x}(PO_4)_3$) *via* mechanical milling and high-temperature (*e.g.*, 500 °C) sintering procedures. Although the resultant high-voltage SSLBs exhibit enhanced capacity and cycling stability, elevated temperatures (*e.g.*, 60 °C) are still required to operate the batteries [23,37,39]. The later approach is to introduce interlayers with high-voltage resistance between the electrodes and PEO-based PEs, increasing the procedures and complexity of the preparation of the PEs and assembly of the batteries [42,46,47,49]. Despite the above-described progress, it is still highly desirable to develop a facile and scalable method to develop PEO-based PEs adaptable to the high-voltage cathodes, making the high-energy-density batteries capable of working at room temperature with enhanced cycling stability.

Herein, we report a scalable one-pot strategy for the preparation of PEO-based PEs with high-voltage compatibility, which can effectively extend the cycle life of 4 V-class SSLBs. The amine-terminated PEO was brought to react with a trimethoxysilane reagent bearing a epoxide group, in the presence of lithium bis(trifluoromethylsulphonyl)imide (LiTFSI) salts and *N*,*N*-dimethylformamide (DMF), *via* a one-pot synthesis process, resulting in the PEO-based PEs comprising covalently cross-linked polymer networks. When taking a high content of LiTFSI salts (70 wt%), LiTFSI-DMF supramolecular aggregates are formed and incorporated in the polymer networks due to the coordination between Li^+ and DMF, making the DMF molecules firmly bound in the resultant PEs. Such a structural feature gives rise to full dissociation of the high content of LiTFSI salts, leading to the high room-temperature ion conductivity (3.4×10^{-4} S/cm) of the PE. More importantly, the high content of dissociated $TFSI^-$ anions are preferentially defluorinated *via* oxidation into lithium fluoride (LiF) on the cathode surface when the battery undergoes charge/discharge cycles, forming a stable and homogeneous cathode electrolyte interface (CEI) on the cathode particles. LiF possesses a wide ESW (0–6.4 V *vs.* Li/Li^+) and low calculated barrier to Li^+ diffusion, which can effectively inhibit the oxidative decomposition of the PEO-based PE, though the PE exhibits an inherent ESW < 4 V. As a result, the high-voltage $LiCoO_2||Li$ battery assembled with the PE exhibits a capacity retention as high as 87.1% after 200 cycles at room temperature at 1 C, enabling the $LiCoO_2||Li$ battery to be cycled at higher rates with superior cycling stability, as compared to the previously reported counterparts. The PEs are also compatible to the nickel-rich layered NCM cathode with higher capacity than the $LiCoO_2$ cathode, making the $NCM_{622}||Li$ battery stably cycled, at room temperature, over 200 cycles at 0.5 C with capacity retention as high as 80.0%. This work provides a scalable method to fabricate PEO-based PEs that are applicable to high-voltage SSLBs, which is expected to improve the energy density of lithium batteries and solve the current "mileage anxiety" problem of the electric vehicles.

Figs. 1a and b present the one-pot preparation process and chemical structure of the PEO-based PEs that are adaptable to the high-voltage cathodes. After dissolving the polyetheramine (Jeffamine), GPTMS and LiTFSI in DMF, the mixture solution was transferred into a Teflon mold and then heated at 80 °C for 3 h, followed by heating the obtained sample at 80 °C for 2 h under vacuum to evaporate the DMF. The molar ratio between the amino groups of Jeffamine and the epoxide groups of GPTMS was fixed at 1:1, while the fraction of LiTFSI in the total mass of Jeffamine, GPTMS and LiTFSI was varied from 30%, 40%, 50%, 60% to 70%. The reaction system involves the following reactions: (1) conjugation between the epoxide groups of GPTMS and the amino groups of Jeffamine *via* the ring-opening reaction, (2) hydrolysis and condensation of the methoxy groups of GPTMS. As a result, the Jeffamine polymer chains are covalently crosslinked by the siloxane groups, while the LiTFSI salts are incorporated into the three-dimensionally crosslinked polymer networks. The as-prepared PEO-based PEs will be denoted as Jef-GPTMS/$LiTFSI_{x\%}$, where x represents the mass fraction of LiTFSI. All the prepared Jef-GPTMS/LiTFSI samples are insoluble in DMF despite swelling observed (Fig. S1 in Supporting information), verifying the formation of covalently crosslinked polymer networks. Fourier transform infrared (FTIR) spectrum of the Jef-GPTMS/$LiTFSI_{70\%}$ sample shows disappearance of both the oxirane ring deformation band (910 cm^{-1}) of the epoxide groups and N–H stretching bands (3300–3400 cm^{-1}) of the primary amine groups, accompanied by the appearance of the N–H stretching band (3247 cm^{-1}) ascribed to the secondary amine groups (Fig. S2 in Supporting information) [53–55]. These results confirm the occurrence of ring-opening reactions between the epoxide and amino groups. TGA indicate that the Jef-GPTMS/$LiTFSI_{x\%}$ samples with higher contents of LiTFSI (x > 50) exhibit noticeable weight losses in the temperature range from 108 °C to 245 °C (Fig. 1c). In contrast, the samples containing lower contents of LiTFSI (x = 30, 40) display little weight loss even up to 330 °C. The above-described weight losses result from the escape of DMF that remained in those samples, which intuitively deviate from the fact that all the samples were heated under vacuum with the purpose of DMF removal. This intriguing phenomenon suggests that DMF is firmly bound in the polymer networks when the LiTFSI fraction is > 50 wt%. Such a deduction can further be verified by the Raman spectroscopy, which shows that the Raman bands assigned to the bound DMF molecules (673 cm^{-1}) are detected for the Jef-GPTMS/$LiTFSI_{60\%}$ and Jef-GPTMS/$LiTFSI_{70\%}$ samples (Fig. 1d) [56,57]. In contrast, neither free (658 cm^{-1}) nor bound DMF are detected for the Jef-GPTMS/LiTFSI samples with lower LiTFSI contents (x = 30, 40) (Fig. 1d), indicating complete removal of DMF in these samples. According to the TGA and Raman characterization, LiTFSI-DMF supramolecular aggregates are formed in the Jef-GPTMS/$LiTFSI_{x\%}$ samples with higher LiTFSI contents (x > 50). The high content of LiTFSI facilitates the coordination between Li^+ and

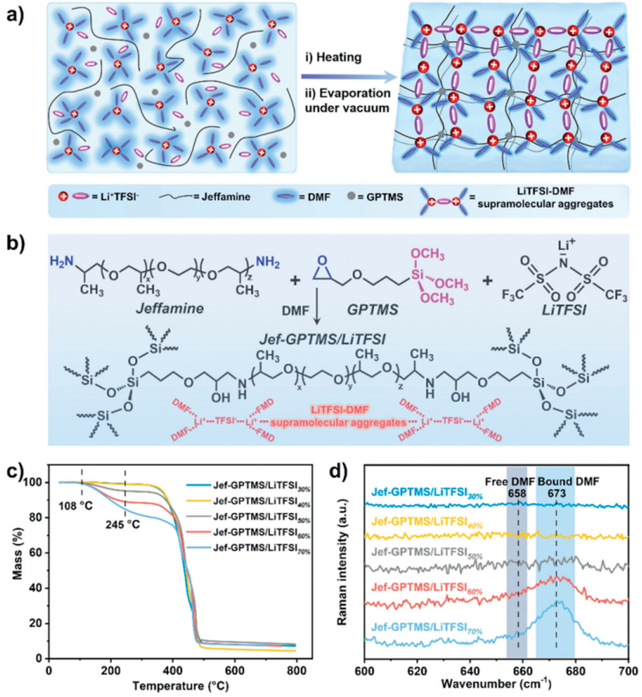

Fig. 1. Schematic illustration of the (a) preparation process and (b) chemical structure of the Jef-GPTMS/LiTFSI PEs. (c) TGA curves and (d) Raman spectra of the different Jef-GPTMS/LiTFSI PEs.

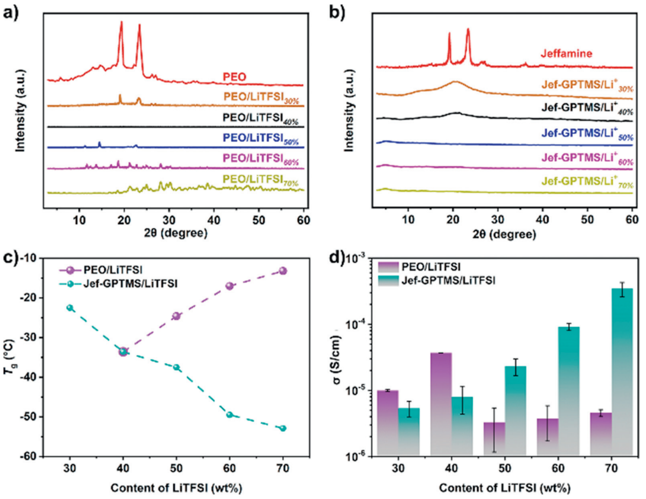

Fig. 2. XRD spectra of the (a) different PEO/LiTFSI and (b) Jef-GPTMS/LiTFSI samples. T_g and room-temperature ionic conductivity of the (c) different PEO/LiTFSI and (d) Jef-GPTMS/LiTFSI samples, as a function of the content of LiTFSI.

the DMF molecules, while the $TFSI^-$ anions enter into the Li^+ ion solvation structure to form the LiTFSI-DMF supramolecular aggregates (Figs. 1a and b) [43,58,59].

As the references of the Jef-GPTMS/LiTFSI PEs, PEO/LiTFSI PEs with different LiTFSI contents were prepared from the mixture solution of PEO and LiTFSI in acetonitrile (see Experimental section in Supporting information). The PEO/LiTFSI samples will be denoted as PEO/LiTFSI$_{x\%}$, where x% represents the mass fraction of LiTFSI in the total mass of PEO and LiTFSI. Crystallinity of the PEO chains in the PEO/LiTFSI and Jef-GPTMS/LiTFSI samples was investigated by the X-ray diffraction (XRD) measurements. The PEO/LiTFSI$_{x\%}$ samples with a lower LiTFSI content ($x = 30$) shows similar crystalline peaks to the pure PEO sample, indicating crystallization of the PEO chains (Fig. 2a). With the increase of the LiTFSI content, the PEO crystalline peaks disappear, whereas the crystalline peaks assigned to the LiTFSI salts appear and become more and more distinct, in the PEO/LiTFSI$_{x\%}$ samples with $x > 50$ (Fig. 2a). These results suggest crystallization of the LiTFSI salts in the PEO/LiTFSI$_{x\%}$ samples with higher LiTFSI contents ($x > 50$) [60]. In sharp contrast, no crystalline peaks are detected for all the Jef-GPTMS/LiTFSI$_{x\%}$ samples, though PEO crystalline peaks are detected in the non-crosslinked Jeffamine (Fig. 2b). Therefore, crystallization of both the PEO chains and LiTFSI salts is effectively inhibited in the Jef-GPTMS/LiTFSI samples, giving rise to high flexibility of the PEO chains and full dissociation of the LiTFSI salts even at high contents. These two effects are highly favorable for the enhancement of the ionic conductivity of the Jef-GPTMS/LiTFSI PEs. Differential scanning calorimetry (DSC) measurements show that the glass transition temperatures (T_g) of the PEO/LiTFSI$_{x\%}$ samples with $x > 40$ increase with the LiTFSI contents (Fig. 2c and Fig. S3a in Supporting information), which is ascribed to the crosslinking of the PEO chains by Li^+ ions [61,62]. Oppositely, T_g of the Jef-GPTMS/LiTFSI samples decreases with the increase of the LiTFSI content (Fig. 2c and Fig. S3b in Supporting information). Meanwhile, the Jef-GPTMS/LiTFSI$_{x\%}$ sample exhibits a much lower T_g compared to the PEO/LiTFSI$_{x\%}$ at a given LiTFSI content, when $x > 50$ (Fig. 2c). These results can be explained by the following reasons: (1) The LiTFSI-DMF supramolecular aggregates play a plasticizing role in the Jef-GPTMS/LiTFSI$_{x\%}$ samples; (2) The strong coordination between Li^+ and DMF attenuates the crosslinking degree of the PEO chains by Li^+ ions. These two effects synergistically increase the mobility of the PEO chains and thus make the T_g of the Jef-GPTMS/LiTFSI$_{x\%}$ samples decreased with the increase of the LiTFSI content.

Fig. 2d depicts the room-temperature ionic conductivity of the Jef-GPTMS/LiTFSI$_{x\%}$ and PEO/LiTFSI$_{x\%}$ samples. The Jef-GPTMS/LiTFSI$_{x\%}$ samples exhibit lower ionic conductivity than the PEO/LiTFSI$_{x\%}$ when $x < 40$, whereas the ionic conductivity of the Jef-GPTMS/LiTFSI$_{x\%}$ samples is much higher than that of the PEO/LiTFSI$_{x\%}$ at higher LiTFSI contents with $x > 50$. Meanwhile, the Jef-GPTMS/LiTFSI electrolyte exhibits monotonically increased ionic conductivity with the increase of the LiTFSI content. The lower T_g and full dissociation of the LiTFSI salts synergistically contribute to the higher ionic conductivity of the Jef-GPTMS/LiTFSI$_{x\%}$ samples with higher LiTFSI contents ($x > 50$). In contrast, the ionic conductivity of the PEO/LiTFSI$_{x\%}$ samples increases and then decreases, because of the crystallization of the LiTFSI salts at higher contents ($x > 50$). The Jef-GPTMS/LiTFSI$_{70\%}$ and PEO/LiTFSI$_{40\%}$ samples exhibit the highest room-temperature ionic conductivity of 3.4×10^{-4} and 3.6×10^{-5} S/cm, among all the Jef-GPTMS/LiTFSI$_{x\%}$ and PEO/TFSI$_{x\%}$ samples, respectively. Moreover, the Jef-GPTMS/LiTFSI$_{70\%}$ electrolyte exhibits much higher ionic conductivity than the PEO/LiTFSI$_{40\%}$ in the whole temperature range from 25 °C to 80 °C (Fig. S4 in Supporting information). Accordingly, the Jef-GPTMS/LiTFSI$_{70\%}$ and PEO/LiTFSI$_{40\%}$ electrolytes are exclusively studied henceforth.

Electrochemical compatibility of the Jef-GPTMS/LiTFSI$_{70\%}$ electrolyte with the Li metal electrode was evaluated by the Li plating/stripping performance in the Li||Li symmetric cell. The Li||Li symmetric cell maintains low overpotentials of 73.5, 136.4, 213 and 292.0 mV at the current densities of 0.05, 0.10, 0.15 and 0.20 mA/cm^2, respectively. Additionally, steady Li striping/plating processes were achieved for 800 h at the current density of 0.10 mA/cm^2, while no Li dendrite-induced short circuits or erratic cycles were observed. These results indicate that the Jef-GPTMS/LiTFSI$_{70\%}$ electrolyte exhibits a long-term electrochemical compatibility and excellent interfacial stability with the Li metal [63–65]. Accordingly, Li metal as the reference and counter electrode can be paired with the traditional $LiFePO_4$ cathode and the high-voltage cathodes to test the electrochemical performance of the Jef-GPTMS/LiTFSI$_{70\%}$ electrolyte. The $LiFePO_4$||Jef-GPTMS/LiTFSI$_{70\%}$||Li cell delivers much higher capacities at room temperature at the different rates up to 4 C than the $LiFePO_4$||PEO/LiTFSI$_{40\%}$||Li battery (Fig. S6a in Supporting information). The $LiFePO_4$||Jef-GPTMS/LiTFSI$_{70\%}$||Li batteries, tested at room temperature, deliver quite steady discharge capacities of *ca.* 146.2 and 133.3 mAh/g at 0.2 C and 0.5 C in the long-term cycling processes up to 213 and 481 cycles, respectively (Figs. S6b and c in Supporting information). However, the $LiFePO_4$||PEO/LiTFSI$_{40\%}$||Li battery exhibits quickly faded discharge capacity which drops to zero after only 20 cycles due to the low room-temperature ionic conductivity of the PEO/LiTFSI$_{40\%}$ (3.6×10^{-5} S/cm) (Fisg. S6b and c). Therefore, 60 °C is chosen as the operation temperature for the $LiFePO_4$||PEO/LiTFSI$_{40\%}$||Li battery. The Jef-GPTMS/LiTFSI$_{70\%}$ electrolyte was further assembled into the high-voltage $LiCoO_2$||Li batteries, which were cycled at the cut-off voltage of 4.3 V. The $LiCoO_2$||Jef-GPTMS/LiTFSI$_{70\%}$||Li cell delivers a high capacity of *ca.* 120.3 mAh/g at room temperature at the rate up to 1 C (Fig. S7 in Supporting information). In contrast, the discharge capacity of the $LiCoO_2$||PEO/LiTFSI$_{40\%}$||Li battery exhibits continuous decay from 0.1 C to 1 C, and drops to zero at 1 C, even at 60 °C (Fig. S7). Fig. 3a shows the cycling performances of the $LiCoO_2$||Jef-GPTMS/LiTFSI$_{70\%}$||Li and $LiCoO_2$||PEO/LiTFSI$_{40\%}$||Li cells. The $LiCoO_2$||Jef-GPTMS/LiTFSI$_{70\%}$||Li cell exhibits excellent cycling performance at room temperature, delivering discharge capacities of 113.0 mAh/g and 98.4 mAh/g at 1 C for the 1st and 200th cycles, respectively. The capacity retention is as high as 87.1% that corresponds to only 0.06% decay per cycle, demonstrating the high compatibility of the Jef-GPTMS/LiTFSI$_{70\%}$ electrolyte to the high-voltage $LiCoO_2$ cathode. The $LiCoO_2$||Li cell exhibits fluctuation in

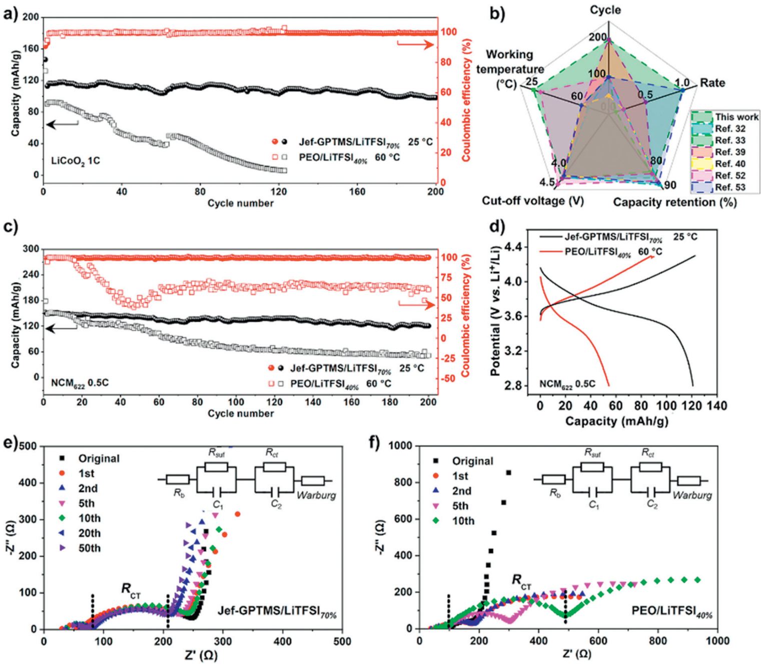

Fig. 3. Cycling performances of the (a) $LiCoO_2$||Li and (c) NCM_{622}||Jef-GPTMS/$LiTFSI_{70\%}$||Li batteries, assembled with the Jef-GPTMS/$LiTFSI_{70\%}$ and PEO/$LiTFSI_{40\%}$ electrolytes, which were cycled at (a) 1 C and (c) 0.5 C at room temperature. (b) Radar chart showing the comparison of the cycling and rate performance, working temperature, and cut-off voltage between the Jef-GPTMS/$LiTFSI_{70\%}$ electrolyte and the previously reported PEO-based PEs for high-voltage SSLBs. (d) Typical galvanostatic charge/discharge voltage profiles of the NCM_{622}||Jef-GPTMS/$LiTFSI_{70\%}$||Li and NCM_{622}||PEO/$LiTFSI_{40\%}$||Li batteries after cycling for 200 cycles at 0.5 C. Nyquist plots of the (e) NCM_{622}||Jef-GPTMS/$LiTFSI_{70\%}$||Li and (f) NCM_{622}||PEO/$LiTFSI_{40\%}$||Li batteries before and after cycling for different cycles at 0.5 C.

the cycling process due to the fluctuation of room temperature. In sharp contrast, the $LiCoO_2$||PEO/$LiTFSI_{40\%}$||Li cell running at 1 C, even tested at the elevated temperature of 60 °C, shows fast capacity fading from 90.4 mAh/g to only 17.1 mAh/g after 100 cycles. Notably, compared to the previously reported PEO-based PEs applied in the $LiCoO_2$||Li batteries, the Jef-GPTMS/$LiTFSI_{70\%}$ electrolyte not only enables the battery to work at the lowest temperature (*i.e.*, room temperature), but also makes the battery exhibit the longest cycling life and the highest rate performance (Fig. 3b and Table S1 in Supporting information) [37,39,47,49,66,67].

The nickel-rich $Li(Ni_xCo_yMn_{1-x-y})O_2$ (NCM, $x \geq 0.6$) is the standard high-voltage cathode material used in electric vehicles, possessing higher capacity than $LiCoO_2$ due to the active Ni (Ni^{2+}) element in the NCM cathode [68]. During the charging process, the oxidation of nickel in the nickel-rich NCM cathode from +2 to +4 with a two-electron transfer offers a higher capacity than that of cobalt oxidized from +3 to +4 in the $LiCoO_2$ cathode. However, it is more challenging to stabilize the electrode-electrolyte interface for the NCM cathode, because of their inferior structural stability compared to the $LiCoO_2$ cathodes during the electrochemical cycling [68]. In this scenario, the Jef-GPTMS/$LiTFSI_{70\%}$ electrolyte is further tested in the high-voltage NCM||Li batteries. The cyclic voltammetry (CV) curves of the NCM_{622}||Jef-GPTMS/$LiTFSI_{70\%}$||Li battery show reversible oxidation and reduction peaks at *ca.* 3.9 V and *ca.* 3.6 V, respectively, well matching the characteristic redox processes of the NCM_{622} cathode (Fig. S8 in Supporting information). The NCM_{622}||Jef-GPTMS/$LiTFSI_{70\%}$||Li battery exhibits discharge capacities of *ca.* 165.4, 158.2, 143.8 and 129.0 mAh/g at the rates of 0.1, 0.2, 0.5 and 1 C at room temperature, respectively (Fig. S9 in Supporting information). Fig. 3c shows that the NCM_{622}||Jef-GPTMS/$LiTFSI_{70\%}$||Li battery, cycled at room temperature, exhibits a capacity retention as high as 80.0% after the long-term cycling for 200 cycles at 0.5 C, and the average coulombic efficiency reaches as high as 99.3%. In sharp contrast, the NCM_{622}||PEO/$LiTFSI_{40\%}$||Li battery, tested even at the elevated temperature of 60 °C, exhibits a much lower capacity retention of only 34.5%, and the coulombic efficiency drops from 94.6% to 60.0% after 200 cycles. The charge/discharge voltage profiles of the two batteries at the 200th cycle show that the NCM_{622}||Jef-GPTMS/$LiTFSI_{70\%}$||Li battery exhibits higher capacity reversibility and lower overpotential (Fig. 3d), verifying its superior cycling performance. Compared to the NCM_{622} cathode, the NCM_{811} cathode with a higher nickel content has a higher theoretical capacity, but it is more difficult to maintain the stable cycling behavior of the NCM_{811} batteries because of the more severe structural disordering of the NCM_{811} cathode material. The compatibility of the Jef-GPTMS/$LiTFSI_{70\%}$ electrolyte with the NCM_{811} cathode was further tested in the NCM_{811}||Li button cells and pouch cells. Encouragingly, the NCM_{811}||Jef-GPTMS/$LiTFSI_{70\%}$||Li button cell delivers a high capacity of *ca.* 102 mAh/g at room temperature at the rate up to 1 C (Figs. S10a and b in Supporting information). The capacity retention of the NCM_{811}||Jef-GPTMS/$LiTFSI_{70\%}$||Li button cell reaches >90% and >80%, after 60 cycles at 0.1 C and after 100 cycles at 0.2 C, respectively (Figs. S10c and d in Supporting information). The NCM_{811}||Jef-GPTMS/$LiTFSI_{70\%}$||Li pouch cell exhibits an open circuit voltage of 4.23 V and retains a high discharge capacity of 127.2 mAh/g after 35 cycles at 0.2 C (Fig. S11 in Supporting information). All these results signify the potential applicability of the Jef-GPTMS/$LiTFSI_{70\%}$ electrolyte in the high-voltage NCM_{811} batteries that have been practically used as the power sources of the electric vehicles. To understand the superior electrochemical performance of the Jef-GPTMS/$LiTFSI_{70\%}$ electrolyte, the impedance evolution of the NCM_{622}||Jef-GPTMS/$LiTFSI_{70\%}$||Li and NCM_{622}||PEO/$LiTFSI_{40\%}$||Li batteries before and after cycling was further evaluated by the electrochemical impedance spectroscopy (EIS). Figs. 3e and f show the Nyquist plots of the NCM_{622}||Jef-GPTMS/$LiTFSI_{70\%}$||Li and NCM_{622}||PEO/$LiTFSI_{40\%}$||Li batteries before and after different cycles at 0.5 C, while the equivalent circuits are used to fit the impedance spectra (insets of Figs. 3e and f). The x-axis intercept of the Nyquist plot can be interpreted as the bulk electrolyte resistance (R_b), the first semicircle is assigned to the resistance ascribed to the Li-ion diffusion through the surface layer (R_{suf}), the second semicircle is ascribed to the charge-transfer resistance (R_{ct}), and the tail line indicates the Warburg resistance (Z_w) (insets of Figs. 3e and f) [69–71]. R_{ct} of the NCM_{622}||Jef-GPTMS/$LiTFSI_{70\%}$||Li battery decreases from 169.1 Ω to 140.4 Ω after 50 cycles (Fig. 3e), whereas the R_{ct} of the NCM_{622}||PEO/$LiTFSI_{40\%}$||Li cell increases drastically from 86.8 Ω to 396.6 Ω after only 10 cycles (Fig. 3f).

These results suggest that the Jef-GPTMS/$LiTFSI_{70\%}$ electrolyte facilitates the formation of a stable electrode-electrolyte interface to promote the Li^+ ion transport. Broadening the ESW of a PE is the most typical strategy to make the PE adaptable to the high-voltage cathode and thus improve the cycling performance of the high-voltage battery [9]. Intriguingly, the Jef-GPTMS/$LiTFSI_{70\%}$ and PEO/$LiTFSI_{40\%}$ electrolytes show similar ESWs < 4.0 V (Fig. S12 in Supporting information). Therefore, the superior performances of the high-voltage $LiCoO_2$||Li and NCM||Li batteries, assembled with the Jef-GPTMS/$LiTFSI_{70\%}$ electrolytes, originate from a different mechanism. Construction of high-quality cathode electrolyte interface (CEI) can effectively prevent the electrolyte from decomposition and enhance the cycling performance of the high-voltage batteries [70,72–74]. To investigate the CEI effect on the NCM_{622} batteries, X-ray photoelectron spectroscopy (XPS) measurements were conducted to study the chemical component evaluation of the NCM_{622} cathodes in the NCM_{622}||Jef-GPTMS/$LiTFSI_{70\%}$||Li and NCM_{622}||PEO/$LiTFSI_{40\%}$||Li batteries after cycling for 10 cycles. The high-resolution C 1s XPS spectrum of the pristine NCM_{622} cathode is deconvoluted into three components (Fig. 4a), originating from the carbonaceous species from the conductive carbon and the main chain of the PVDF binder (284.3 eV, C–C) [10,75], and the -CH_2 and -CF_2 groups from the PVDF binder (285.8/290.6 eV, C–H/C-F). Compared with the pristine NCM_{622} cathode, the C 1s spectrum of the NCM_{622} cathode, obtained from the cycled NCM_{622}||Jef-GPTMS/$LiTFSI_{70\%}$||Li battery, exhibits following changes (Fig. 4b): (1) The C-F signal (290.6 eV) assigned to the -CF_2 groups from the PVDF binder disappears, accompanied by the appearance of the C-F signal (292.2 eV) assigned to the -CF_3 groups from the adsorbed $TFSI^-$ anions [76–78]; (2) The C–H signal is covered by the emerging C–O signal attributed to the decomposition products from the ether chain (-C-O–C-) of the Jef-GPTMS/$LiTFSI_{70\%}$ electrolyte [76–78]. In the case of the NCM_{622}||PEO/$LiTFSI_{40\%}$||Li battery, the following differences are observed (Fig. 4c): (1) No -CF_3 group from the $TFSI^-$ anions is detected, suggesting no $TFSI^-$ anions are adsorbed on the NCM_{622} cathode surface; (2) The area ratio between the C–O and C–C peaks is much higher, indicating more decomposition products from the PEO/$LiTFSI_{40\%}$ electrolyte are formed on the NCM_{622} cathode surface [77]. The F 1s XPS signal of the pristine NCM_{622} cathode originates solely from the C-F groups from the PVDF binder or $TFSI^-$ anions (Fig. 4d) [23]. Comparatively, except for the C-F signal, the signal assigned to LiF is detected on the NCM_{622} cathode obtained from the cycled NCM_{622}||Jef-GPTMS/$LiTFSI_{70\%}$||Li battery (Fig. 4e) [23,76]. This result indicates that a protective CEI mainly composed of LiF is formed on the NCM_{622} cathode, which is derived from the defluorination of the $TFSI^-$ anions due to oxidation on the cathode. In contrast, no LiF is detected on the NCM_{622} cathode in the case of the NCM_{622}||PEO/$LiTFSI_{40\%}$||Li battery (Fig. 4f). Moreover, the signal-to-noise ratio of the corresponding C-F signal is relatively low, suggesting the accumulation of thick decomposition products from the PEO/$LiTFSI_{40\%}$ electrolyte on the cathode. Therefore, the protective CEI can effectively shield the active NCM_{622} cathode from the Jef-GPTMS/$LiTFSI_{70\%}$ electrolyte, which makes the electrolyte adaptable to the high-voltage cathode, though its ESW is < 4 V [43]. According to the composition and structure of the Jef-GPTMS/$LiTFSI_{70\%}$ electrolyte, the following mechanism is proposed to explain the formation of the protective CEI. The Jef-GPTMS/$LiTFSI_{70\%}$ electrolyte, embedding the LiTFSI-DMF supramolecular aggregates with high content of fully dissociated LiTFSI, facilitates the $TFSI^-$ anions to enter the Helmholtz layer close to the cathode [43,58,59]. Consequently, the $TFSI^-$anions are preferentially defluorinated into LiF *via* oxidation, on the cathode in the course of charge/discharge cycling of the battery [72,79,80]. Because LiF possesses a wide ESW (0–6.4 V *vs.* Li/Li^+) and low calculated barrier to Li diffusion [81–83], the protective CEI effectively stabilizes the electrode-electrolyte interface and facilitates homogeneous Li^+ flux across the electrode-electrolyte interface.

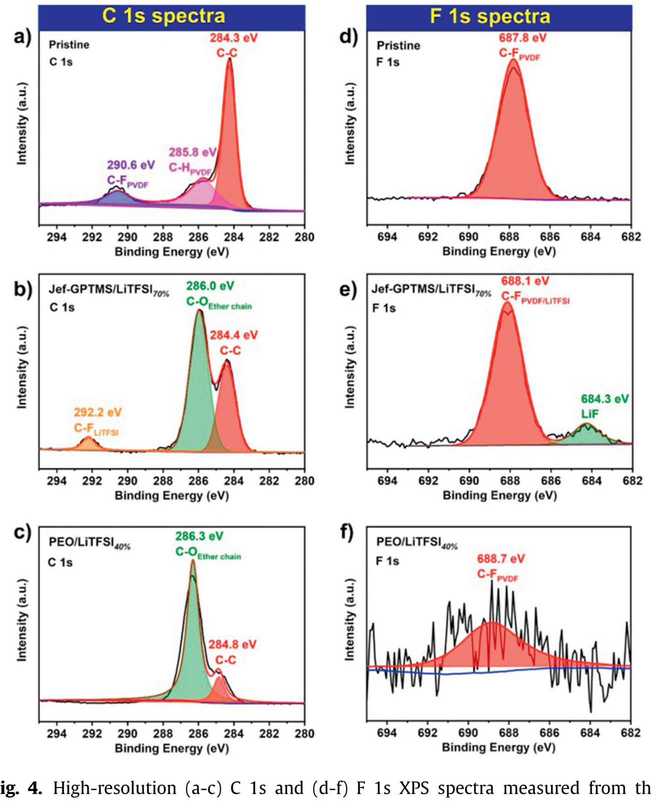

Fig. 4. High-resolution (a-c) C 1s and (d-f) F 1s XPS spectra measured from the surface of the (a, d) pristine NCM_{622} cathode, and those obtained from the cycled NCM_{622}||Li batteries, assembled with the (b, e) Jef-GPTMS/$LiTFSI_{70\%}$ and (c, f) PEO/$LiTFSI_{40\%}$ electrolytes.

Transmission electron microscope (TEM) characterization provides more evidence of the protective CEI on the NCM_{622} cathode in the NCM_{622}||Jef-GPTMS/$LiTFSI_{70\%}$||Li battery. As shown in Fig. 5a, a thin and homogeneous amorphous CEI layer with thickness of *ca.* 2.9 nm was observed under TEM on the surface of the NCM_{622} particle obtained from the cycled NCM_{622}||Jef-GPTMS/$LiTFSI_{70\%}$||Li battery. On the one hand, the thin and homogeneous CEI layer is essential for achieving low interfacial resistance to ensure fast Li^+ ion transportation across the NCM_{622} cathode and the electrolyte, allowing uniform lithiation and de-lithiation (Fig. 5b) [80,84]. On the other hand, the homogeneous CEI, mainly composed of LiF with high-voltage resistance, plays a protective role on the NCM_{622} cathode to effectively inhibit the decomposition of the Jef-GPTMS/$LiTFSI_{70\%}$ electrolyte (Fig. 5b). These effects synergistically make the Jef-GPTMS/$LiTFSI_{70\%}$ electrolyte adaptable to the high-voltage cathode, giving rise to the excellent cycling performance of the high-voltage Li batteries at room temperature. In sharp contrast, the NCM_{622} particle, obtained from the cycled NCM_{622}|| PEO/$LiTFSI_{40\%}$||Li battery, is coated with a thick and inhomogeneous CEI layer (Fig. 5c), resulting from the continuous decomposition of the PEO/$LiTFSI_{40\%}$ electrolyte on the cathode sur-

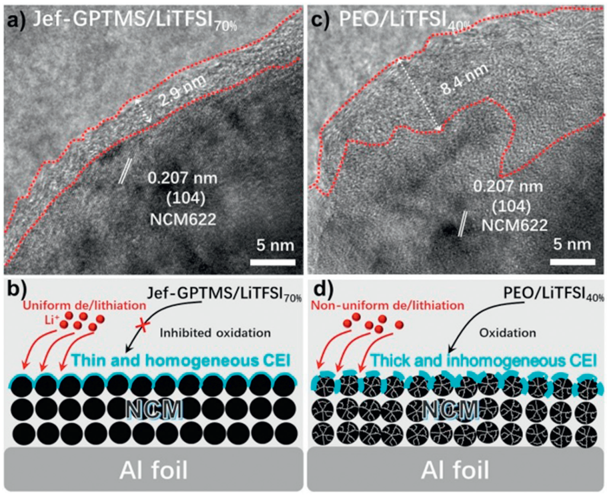

Fig. 5. TEM images of the NCM_{622} particles, obtained from the NCM_{622}||Li batteries after 10 cycles, assembled with the (a) Jef-GPTMS/$LiTFSI_{70\%}$ and (c) PEO/$LiTFSI_{40\%}$ electrolytes. Schematic illustration of the conformation of the CEIs in the NCM_{622}||Li batteries assembled with the (b) Jef-GPTMS/$LiTFSI_{70\%}$ and (d) PEO/$LiTFSI_{40\%}$ electrolytes, and the different effects of the CEIs on the electrode-electrolyte interfaces in the batteries.

face. As shown in Fig. 5d, the inhomogeneous CEI on the NCM_{622} cathode results in non-uniform lithiation/de-lithiation across the cathode-electrolyte interface, which can trigger the fragmentation of the NCM_{622} particles due to the anisotropic strain change. Consequently, the PEO/$LiTFSI_{40\%}$ electrolyte can be continuously oxidized on the cathode, leading to the accumulation of resistive byproducts on the NCM_{622} cathode and degradation of the cycling performance of the battery.

In summary, we have reported a scalable method for the fabrication of PEO-based PEs with high room-temperature ionic conductivity and high-voltage compatibility. The reported Jef-GPTMS/$LiTFSI_{70\%}$ electrolyte was prepared by a one-pot synthesis procedure that involves covalently crosslinking the PEO chains, in the presence of high-content LiTFSI salts and DMF. LiTFSI-DMF supramolecular aggregates are formed and firmly embedded in the polymer network, making the high-content LiTFSI salts fully dissociated and meanwhile suppressing the crystallization of the PEO chains. As a result, the Jef-GPTMS/$LiTFSI_{70\%}$ electrolyte exhibits a room-temperature ionic conductivity as high as 3.4×10^{-4} S/cm. Importantly, the dissociated and highly concentrated $TFSI^-$ anions can enter the Helmholtz layer close to the high-voltage cathode, and are preferentially defluorinated *via* oxidation into LiF, leading to the formation of a thin and homogeneous CEI on the cathode. The CEI mainly composed of LiF not only shields the cathode from the PE to effectively inhibit the oxidation of the PE, but also facilitates uniform lithiation and de-lithiation across the cathode-electrolyte interface. These collective effects make the Jef-GPTMS/$LiTFSI_{70\%}$ electrolyte adaptable to the high-voltage $LiCoO_2$ and NCM cathodes. The $LiCoO_2$||Li battery exhibits a long-term stable cycling performance with capacity retention as high as 87.1% after 200 cycles, at room temperature. Encouragingly, the NCM_{622}||Li battery with higher capacity than the $LiCoO_2$||Li, can also be stably cycled with capacity retention as high as 80.0% after 200 cycles at 0.5 C at room temperature. Different from the strategy to broaden the ESW of a PE, this work provides a new mechanism for the construction of an effective CEI to stabilize the cathode-PE interface in the high-voltage Li batteries. The as-developed Jef-GPTMS/$LiTFSI_{70\%}$ electrolyte shows high promise for the practical application in the high-voltage SSLBs with high energy density to solve the current "mileage anxiety" problem of the electric vehicles.

Declaration of competing interest

The authors declare that they have no known competing financial interests or personal relationships that could have appeared to influence the work reported in this paper.

Acknowledgment

The authors thank the National Key R&D Program of China (No. 2018YFC1105401) for the financial support.

Supplementary materials

Supplementary material associated with this article can be found, in the online version, at doi:10.1016/j.cclet.2023.108482.

References

[1] A. Miura, N.C. Rosero-Navarro, A. Sakuda, et al., Nat. Rev. Chem. 3 (2019) 189–198.
[2] S. Randau, D.A. Weber, O. Koetz, et al., Nat. Energy 5 (2020) 259–270.
[3] L. Zhou, C.Y. Kwok, A. Shyamsunder, et al., Energy Environ. Sci. 13 (2020) 2056–2063.
[4] Y. Ma, J. Wan, Y. Yang, et al., Adv. Energy Mater. 12 (2022) 2103720.
[5] J. Liang, J. Luo, Q. Sun, et al., Energy Storage Mater. 21 (2019) 308–334.
[6] S. Li, S.Q. Zhang, L. Shen, et al., Adv. Sci. 7 (2020) 1903088.
[7] Q. Yu, K. Jiang, C. Yu, et al., Chin. Chem. Lett. 32 (2021) 2659–2678.
[8] T.J. Cai, Y.H. Lo, J.J. Wu, Mater. Today Energy 13 (2019) 119–124.
[9] J. Li, Y. Cai, H. Wu, et al., Adv. Energy Mater. 11 (2021) 2003239.
[10] C.Z. Zhao, Q. Zhao, X. Liu, et al., Adv. Mater. 32 (2020) 1905629.
[11] Q. Zhao, S. Stalin, C.Z. Zhao, et al., Nat. Rev. Mater. 5 (2020) 229–252.
[12] Y. Hu, N. Dunlap, H. Long, et al., CCS Chem. 3 (2021) 2762–2770.
[13] J. Wang, S. Li, Q. Zhao, et al., Adv. Funct. Mater. 31 (2021) 1616.
[14] C. Zhang, T. Jin, G. Cheng, et al., J. Mater. Chem. A 9 (2021) 13388–13401.
[15] M.J. Lee, J. Han, K. Lee, et al., Nature 601 (2022) 217.
[16] J. Ding, R. Xu, C. Yan, et al., Chin. Chem. Lett. 31 (2020) 2339–2342.
[17] G. Xi, M. Xiao, S. Wang, et al., Adv. Funct. Mater. 31 (2021) 2007598.
[18] C. Yang, Q. Wu, W. Xie, et al., Nature 598 (2021) 590.
[19] Y. Zhu, J. Cao, H. Chen, et al., J. Mater. Chem. A 7 (2019) 6832–6839.
[20] M. Ge, X. Zhou, Y. Qin, et al., Chin. Chem. Lett. 33 (2022) 3894–3898.
[21] Y. Na, Z. Chen, Z. Xu, et al., Chin. Chem. Lett. 33 (2022) 4037–4042.
[22] J.R. Nair, L. Imholt, G. Brunklaus, et al., Electrochem. Soc. Interface 28 (2019) 55–61.
[23] J. Lu, J. Zhou, R. Chen, et al., Energy Storage Mater. 32 (2020) 191–198.
[24] X. Cheng, J. Pan, Y. Zhao, et al., Adv. Energy Mater. 8 (2018) 1614.
[25] M. Li, J. Lu, Z. Chen, et al., Adv. Mater. 30 (2018) 1800561.
[26] X. Yu, J. Li, A. Manthiram, ACS Mater. Lett. 2 (2020) 317–324.
[27] Q. Ma, X. Zhang, A. Wang, et al., Adv. Funct. Mater. 30 (2020) 2002824.
[28] Y. Miao, P. Hynan, A. von Jouanne, et al., Energies 12 (2019) 1074.
[29] X. Yuan, F. Ma, L. Zuo, et al., Electrochem. Energy Rev. 4 (2021) 1–34.
[30] W. Wu, Y. Bai, X. Wang, et al., Chin. Chem. Lett. 32 (2021) 1309–1315.
[31] J.T. Hu, J.G. Zhang, Chin. J. Struct. Chem. 38 (2019) 2005–2008.
[32] Y. Lu, Y. Zhang, Q. Zhang, et al., Particuology 53 (2020) 1–11.
[33] X. Xu, S. Lee, S. Jeong, et al., Mater. Today 16 (2013) 487–495.
[34] W.H. Li, H.J. Liang, X.K. Hou, et al., J. Energy Chem. 50 (2020) 416–423.
[35] J. Liu, X. Shen, J. Zhou, et al., ACS Appl. Mater. Interfaces 11 (2019) 45048–45056.
[36] Y. Wang, S. Chen, Z. Li, et al., Energy Storage Mater. 45 (2022) 474–483.
[37] Z. Li, A. Li, H. Zhang, et al., Nano Energy 72 (2020) 104655.
[38] S. Bag, C. Zhou, P.J. Kim, et al., Energy Storage Mater. 24 (2020) 198–207.
[39] J. Qiu, X. Liu, R. Chen, et al., Adv. Funct. Mater. 30 (2020) 1909392.
[40] J.Y. Liang, X.D. Zhang, Y. Zhang, et al., J. Am. Chem. Soc. 143 (2021) 16768–16776.
[41] S. Mao, Z. Shen, W. Zhang, et al., Adv. Sci. 9 (2022) 2104841.
[42] M. Arrese-Igor, M. Martinez-Ibanez, E. Pavlenko, et al., ACS Energy Lett. 7 (2022) 1473–1480.
[43] W. Zhang, Y. Lu, L. Wan, et al., Nat. Commun. 13 (2022) 2041-1723.
[44] D. Zhang, Z. Liu, Y. Wu, et al., Adv.Sci. 9 (2022) 2104277.
[45] L. Li, Y. Deng, H. Duan, et al., J. Energy Chem. 65 (2022) 319–328.
[46] J.Y. Liang, X.X. Zeng, X.D. Zhang, et al., J. Am. Chem. Soc. 141 (2019) 9165–9169.
[47] C. Wang, T. Wang, L. Wang, et al., Adv. Sci. 6 (2019) 1901036.
[48] M. Zhu, J. Wu, B. Liu, et al., J. Membr. Sci. 588 (2019) 117194.
[49] W. Zhou, Z. Wang, Y. Pu, et al., Adv. Mater. 31 (2019) 1805574.
[50] B. Zhao, L. Ma, K. Wu, et al., Chin. Chem. Lett. 32 (2021) 125–131.
[51] L. Li, J. Wang, L. Zhang, et al., Energy Storage Mater. 45 (2022) 1062–1073.
[52] L. Li, H. Duan, L. Zhang, et al., J. Mater. Chem. A 10 (2022) 20331–20342.
[53] H. Abdollahi, A. Salimi, M. Barikani, et al., J. Appl. Polym. Sci. 136 (2019) 47121.
[54] T. Na, H. Jiang, L. Zhao, et al., RSC Adv. 7 (2017) 53970–53976.
[55] G. Nikolic, S. Zlatkovic, M. Cakic, et al., Sensors 10 (2010) 684–696.
[56] L. Liu, D. Zhang, J. Zhao, et al., ACS Appl. Energy Mater. 5 (2022) 2484–2494.
[57] X. Zhang, J. Han, X. Niu, et al., Batter. Supercaps 3 (2020) 876–883.

[58] J. Zheng, J.A. Lochala, A. Kwok, et al., Adv. Sci. 4 (2017) 1700032.
[59] T. Li, X.Q. Zhang, N. Yao, et al., Angew. Chem. Int. Ed. 60 (2021) 22683–22687.
[60] X. Wang, Y. Zhang, X. Zhang, et al., ACS Appl. Mater. Interfaces 10 (2018) 24791–24798.
[61] V. Vijayakumar, D. Diddens, A. Heuer, et al., ACS Appl. Mater. Interfaces 12 (2020) 567–579.
[62] Z. Hu, J. Chen, Y. Guo, et al., J. Membr. Sci. 599 (2020) 117827.
[63] J. Castillo, A. Santiago, X. Judez, et al., Chem. Mater. 33 (2021) 8812–8821.
[64] P. Yu, Y. Ye, J. Zhu, et al., Front. Chem. 9 (2021) 786956.
[65] Q. Ke, Q. Xu, X. Lai, et al., Chin. Chem. Lett. 12 (2022) 22–48.
[66] J. Bae, X. Zhang, X. Guo, et al., Nano Lett. 21 (2021) 1184–1191.
[67] Z. Lv, Q. Zhou, S. Zhang, et al., Energy Storage Mater. 37 (2021) 215–223.
[68] X. Wang, Y.L. Ding, Y.P. Deng, et al., Adv. Energy Mater. 10 (2020) 1903864.
[69] W. Choi, H.C. Shin, J.M. Kim, et al., J. Electrochem. Sci. Technol. 11 (2020) 1–13.
[70] J. Lei, X.X. Fan, T. Liu, et al., Nat. Commun. 13 (2022) 202.
[71] J. Oh, S.H. Choi, B. Chang, et al., ACS Energy Lett. 7 (2022) 1374–1382.
[72] P. Bai, X. Ji, J. Zhang, et al., Angew. Chem. Int. Ed. 134 (2022) 202202731.
[73] D. Wu, J. He, J. Liu, et al., Adv. Energy Mater. 12 (2022) 2200337.
[74] S. Kim, S.O. Park, M.Y. Lee, et al., Energy Storage Mater. 45 (2022) 1–13.
[75] J. Oh, J. Kim, Y.M. Lee, et al., Mater. Chem. Phys. 222 (2019) 1–10.
[76] B. Flamme, J. Swiatowska, M. Haddad, et al., J. Electrochem. Soc. 167 (2020) 070508.
[77] S. Jiao, X. Ren, R. Cao, et al., Nat. Energy 3 (2018) 739–746.
[78] X. Yang, M. Jiang, X. Gao, et al., Energy Environ. Sci. 13 (2020) 1318–1325.
[79] J. Fu, X. Ji, J. Chen, et al., Angew. Chem. Int. Ed. 59 (2020) 22194–22201.
[80] W. Liu, J. Li, W. Li, et al., Nat. Commun. 11 (2020) 3629.
[81] X. Ren, L. Zou, S. Jiao, et al., ACS Energy Lett. 4 (2019) 896–902.
[82] M. He, R. Guo, G.M. Hobold, et al., Proc. Natl. Acad. Sci. U. S. A. 117 (2020) 73–79.
[83] J. Ko, Y.S. Yoon, Ceram. Int. 45 (2019) 30–49.
[84] Y. Ma, J. Ma, J. Chai, et al., ACS Appl. Mater. Interfaces 9 (2017) 41462–41472.